

Observation of Standing Slow Magneto-acoustic Waves in a Flaring Active Region Corona Loop

A. Abedini

Department of Physics, University of Qom, Qom University Blvd Alghadir, P.O. Box 3716146611, Qom, Iran; a.abedini@qom.ac.ir Received 2024 July 13; revised 2024 September 7; accepted 2024 September 11; published 2024 October 9

Abstract

Intensity fluctuations are frequently observed in different regions and structures of the solar corona. These fluctuations may be caused by magneto-hydrodynamic (MHD) waves in coronal plasma. MHD waves are prime candidates for the dynamics, energy transfer, and anomalous temperature of the solar corona. In this paper, analysis is conducted on intensity and temperature fluctuations along the active region coronal loop (NOAA AR 13599) near solar flares. The intensity and temperature as functions of time and distance along the loop are extracted using images captured by the Atmospheric Imaging Assembly (AIA) instrument onboard the Solar Dynamics Observatory (SDO) space telescope. To observe and comprehend the causes of intensity and temperature fluctuations, after conducting initial processing, and applying spatial and temporal frequency filters to data, enhanced distance-time maps of these variables are drawn. The space-time maps of intensities show standing oscillations at wavelengths of 171, 193, and 211 Å with greater precision and clarity than earlier findings. The amplitude of these standing oscillations (waves) decreases and increases over time. The average values of the oscillation period, damping time, damping quality, projected wavelength, and projected phase speed of standing intensity oscillations are in the range of 15–18 minutes, 24-31 minutes, 1.46''-2'', 132''-134'', and 81-100 km s⁻¹, respectively. Also, the differential emission measure peak temperature values along the loop are found in the range of 0.51-3.98 MK, using six AIA passbands, including 94, 131, 171, 193, 211, and 335 Å. Based on the values of oscillation periods, phase speeds, damping time, and damping quality, it is inferred that the fluctuations in intensity are related to standing slow magneto-acoustic waves with weak damping.

Key words: magnetohydrodynamics (MHD) – waves – Sun: corona – Sun: atmosphere – Sun: flares

1. Introduction

In recent decades, the deployment of terrestrial and solar space telescopes with high temporal and spatial resolution has led to the frequent observation of periodic and quasi-periodic intensity fluctuations in various regions and structures of the solar corona (e.g., Ofman et al. 1997; DeForest & Gurman 1998; Wang et al. 2009a, 2009b; Krishna Prasad et al. 2014; Abedini 2016, 2021; Pant et al. 2017). Often, magneto-hydrodynamic (MHD) (fast and slow) waves have been interpreted as the cause of these oscillations. MHD waves are believed to play an important role in the dynamics (Aschwanden 2009) and coronal heating (Ofman 2005; Taroyan & Erdélyi 2009). By measuring the parameters of the observational MHD waves and aligning them with theoretical models, the physical parameters of coronal plasma like magnetic field (Aschwanden et al. 2002; Wang et al. 2007), gravitational stratification (Andries et al. 2005; Van Doorsselaere et al. 2008), and temperature (Marsh et al. 2009; Wang et al. 2009a) can be extracted. The intensity disturbances in the solar corona with oscillation periods of about one minute or less are primarily attributed to fast MHD waves (Kupriyanova et al. 2013). In contrast, disturbances with oscillation periods of about 10 minutes or longer are explained as slow MHD waves (Van Doorsselaere et al. 2011). Some authors believe that slow magneto-acoustic waves (compression or longitudinal waves) in the solar plasma are responsible for intensity oscillations (propagation or standing) with long oscillation periods and speeds of roughly several tens of kilometers per second (Banerjee et al. 2007; Wang 2011; Jiao et al. 2015; Pant et al. 2015, 2017; Samanta et al. 2015; Yuan et al. 2015; Abedini 2016, 2021; Bryans et al. 2016). Today, there are numerous observations of magneto-acoustic processes occurring in various solar corona structures such as polar plumes, polar coronal holes, flaring fan loops, and non-flaring fan coronal loops (open and closed). Also, there are many theoretical and observational studies about the excitation, damping, and parameters of propagating and standing magneto-acoustic waves in different regions and structures of the solar corona.

For instance, Ofman et al. (1997) and DeForest & Gurman (1998) first observed intensity disruptions in the polar coronal hole regions using Ultraviolet Coronagraph Spectrometer (UVCS) and Extreme ultraviolet Imaging Telescope (EIT) onboard the Solar and Heliospheric Observatory (SOHO). Ofman et al. (1999) interpreted these propagation disturbances

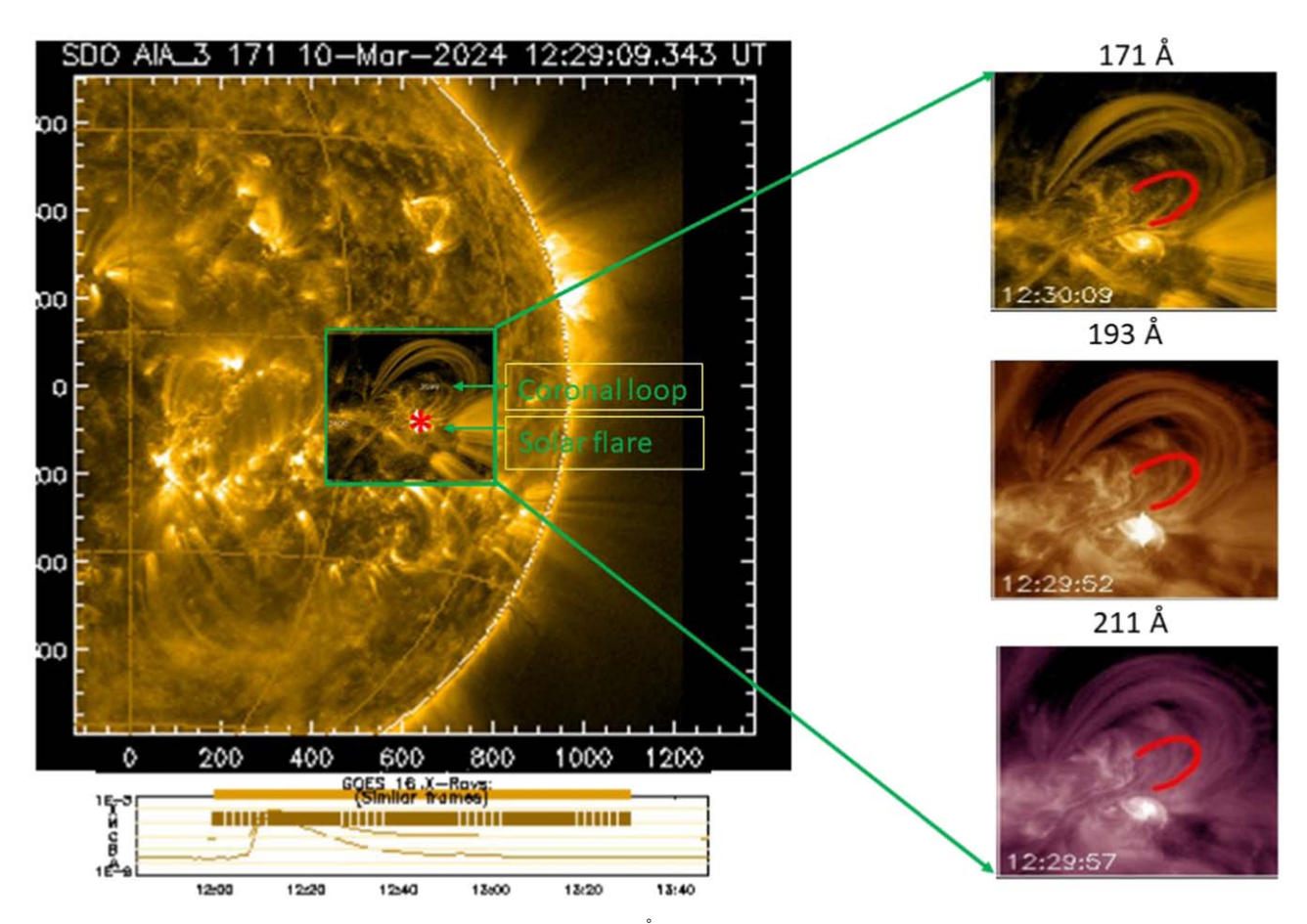


Figure 1. On the left, a snapshot of the Sun at 12:29:09 UT in Channel 171 Å on 2024 March 10th is depicted. A green rectangle marks the area of interest, encompassing AR 13599, M-class solar flares, and a series of loops adjacent to the flares. The right side shows a magnified view of the green rectangle in 171, 193 and 211 Å, focusing on a thin closed loop (red line) located near the flare. The path of the loop is joined by successive macropixels (cells), 3×3 pixels in size along the loop strands for analysis. The mean intensity of these cells as a function of time is extracted to identify longitudinal standing oscillations.

as magneto-acoustic waves. Intensity oscillations in polar coronal holes were first detected through UVCS by Ofman et al. (1997). They suggested that these oscillations were due to slow magneto-acoustic modes in those areas. The same propagating disruptions were promptly identified as magnetoacoustic waves propagating in the coronal loops by Berghmans & Clette (1999) using EIT/SOHO, Nightingale et al. (1999) and De Moortel et al. (2000) with Transition Region and Coronal Explorer (TRACE) onboard SOHO. Kumar et al. (2013, 2015), Wang et al. (2015), Mandal et al. (2016), Nisticò et al. (2017) have reported findings of both propagating and standing slow waves at hot coronal loop locations near solar flares. They used X-Ray Telescope (XRT) images from the Hinode spacecraft and Atmospheric Imaging Assembly (AIA) images from the Solar Dynamics Observatory (SDO). These investigations disclosed that flares near the base of hot coronal loops not only produce propagating slow magneto-acoustic waves, but also lead to standing slow waves. Wang et al. (2002) detected oscillations in Doppler velocity and intensity disturbances of Fe XIX emission lines in hot coronal loops near

flares with the Solar Ultraviolet Measurements of Emitted Radiation (SUMER) instrument on SOHO, and the Soft X-Ray Telescope (SXT) instrument on the Yohkoh spacecraft. These oscillations, with periods ranging from 14 to 18 minutes, were interpreted as standing slow modes. Wang et al. (2003a, 2003b) conducted statistical studies on the intensity disturbance and Doppler velocity in several post-flare coronal hot loops (T > 6 MK). They found a $\pi/2$ phase difference between Doppler velocity and intensity fluctuations in the Fe XIX and Fe XXI emission lines. They claimed that this phase difference indicates the presence of longitudinal standing slow oscillation modes in the solar corona (also see Wang 2011; Yuan et al. 2015). Pant et al. (2017) observed standing slow waves in fanlike loops near flares using AIA/SDO. Yuan et al. (2015) simulated the generation of slow waves in the coronal loops near solar flares. Their findings indicated that the standing slow waves should also be detectable in addition to the propagating slow waves.

Today, there are varying views on the excitation of magnetic-acoustic waves. Some suggest that standing slow

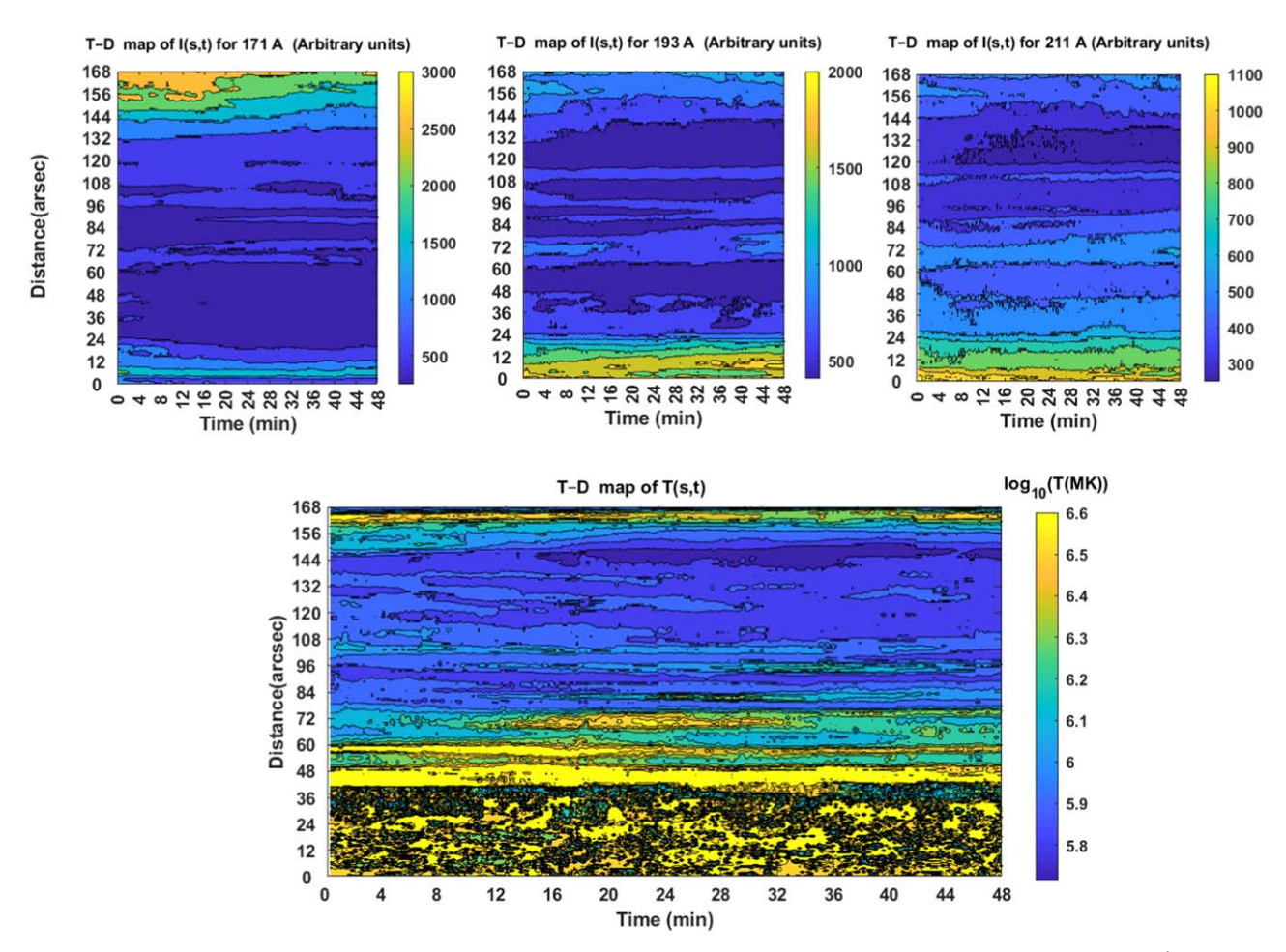


Figure 2. Space-time maps showing the intensities of macropixels with size 3×3 pixels on the loop strands for wavelengths 171, 193, and 211 Å (top row). Space-time map showing the DEM peak temperature of the strips along the selected loop, derived from DEM analysis method (bottom row).

waves arise from the momentum generated by solar flare energy. Flare-induced heat leads to asymmetric heating at one footpoint of the coronal loop, giving rise to standing slow waves within them.

For example, Wang et al. (2005) examined standing waves in hot coronal loops. They asserted that the standing waves in the loops are quickly generated because of the asymmetric heating of the footpoints, triggered by flare energy, and are subsequently damped over about one oscillation period. Selwa et al. (2005) conducted a numerical study on hot loops, demonstrating that gas pressure pulses released from flares near the loop's base generate the first harmonic mode of a slow wave, while pulses near the apex induce the second harmonic mode. However, Tsiklauri et al. (2004) conducted a statistical study on longitudinal fluctuations. The results revealed that the excitation of the second harmonic standing oscillations near the apex is independent of the heating location caused by a flare in the coronal loops. Taroyan et al. (2005, 2007) conducted onedimensional (1D) MHD simulations of slow modes, demonstrating that impulsive footpoint heating can induce standing

slow waves. In subsequent work, Taroyan et al. (2007) and Taroyan & Bradshaw (2008) developed a 1D MHD model to differentiate between standing and propagating slow oscillations in both hot and cool coronal loops. They observed that the intensity phase of the oscillation consistently evolves as a function of time due to loop heating and cooling. They claimed that the best way to distinguish between propagating and standing waves is through the phase difference between the intensity and the Doppler oscillations. Yuan et al. (2015) studied an enhanced model examining the generation of slow magneto-acoustic modes in hot flare loops. They demonstrated that amplitude variation along the coronal loops signifies the presence of such waves. The results of the observations indicate that propagating and standing magneto-acoustic waves often experience rapid damping.

Various factors like thermal conductivity, radiation, and compressive viscosity contribute to the damping of magneto-acoustic waves. Early theoretical studies suggest that thermal conduction plays a key role in the strong damping of slow magneto-acoustic waves (Ofman & Wang 2002). However,

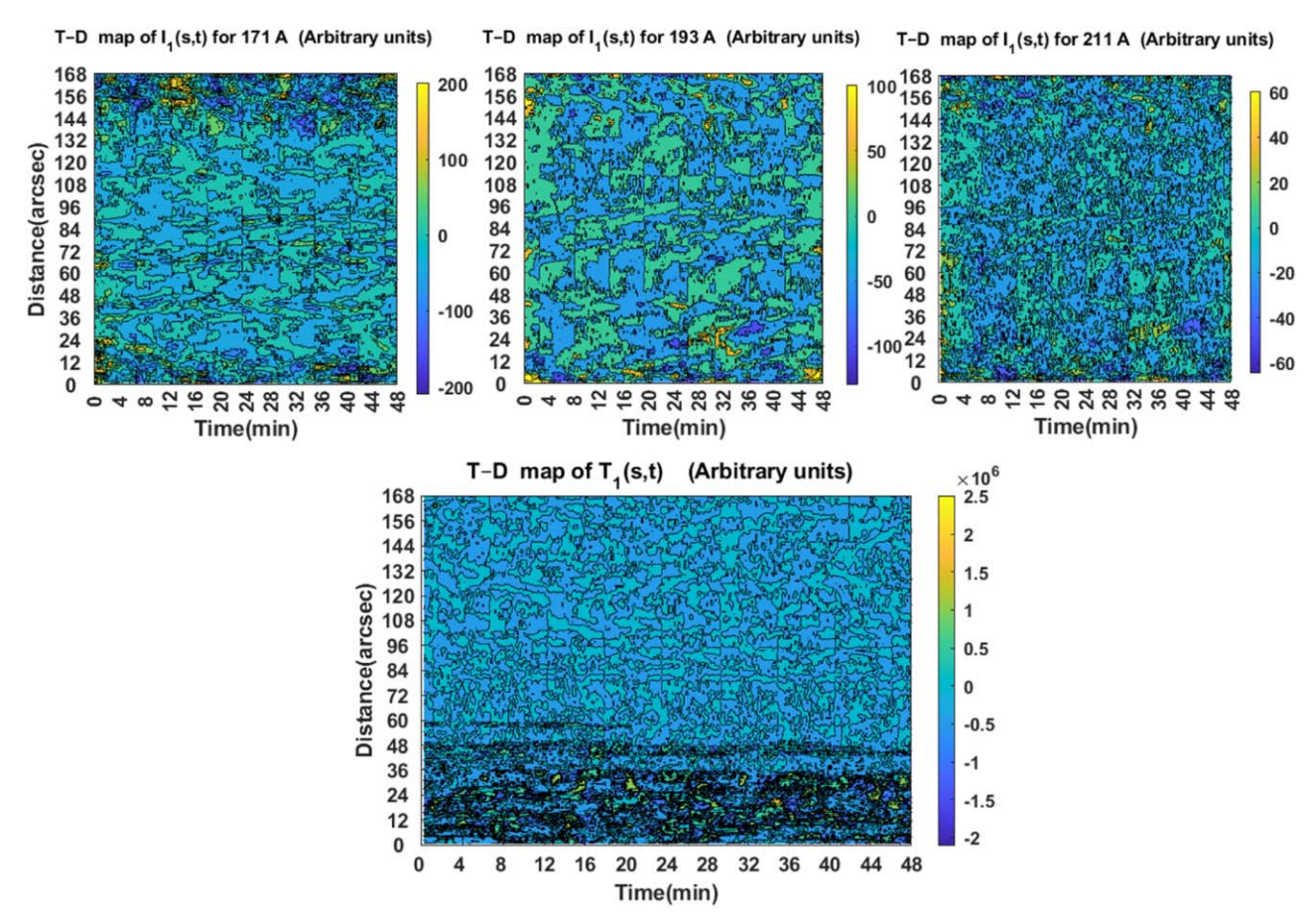


Figure 3. Space-time maps show the background-subtracted intensities of macropixels in channels 171 Å, 193 Å, and 211 Å (top row). The bottom row shows the space-time map of the background-subtracted DEM peak temperature of the strips along the coronal loop.

subsequent analyses and numerical simulations have shown that thermal conductivity alone may not be the primary damping factor for slow oscillations (Sigalotti et al. 2007; Abedini & Safari 2011; Abedini et al. 2012; Wang et al. 2015).

Magneto-acoustic waves have often been observed in hot coronal loops, but standing magneto-acoustic waves, especially in closed and cold coronal loops, have been rarely reported.

This study aims to improve the detection of standing slow waves in a closed and cold thin coronal loop near solar flares. Standing slow magneto-acoustic waves were observed to be more precise and clearer compared to earlier findings. Physical quantities related to these fluctuations were calculated and analyzed.

This paper is organized as follows: Section 2 describes the observations. Section 3 addresses the method of data analysis. The discussion and conclusion are presented in Section 4.

2. Observations

On 2024 March 10, between 12:00 and 13:30, 450 sequential images taken by the AIA/SDO tool with 12 s intervals in

channels 94 Å (Fe XVIII), 131 Å (Fe XX), 171 Å (Fe IX), 193 Å (Fe IXV), 211 Å (Fe XIV), and 335 Å (Fe XVI) were selected from a series of loops located in the active region NOAA AR 13599 close to the associated solar flares. A thin closed coronal loop, roughly 175" long, positioned near and suitably related to the solar flares, was chosen. For example, in Figure 1, a sample of 450 consecutive images whose characteristics are written at the top of the image is displayed. On the left side of Figure 1, it shows an image of the Sun at 12:29:09 UT in Channel 171 Å on the 10th of March, 2024. The area of interest, which is marked with a green rectangle, includes active region numbered 13599, M-class solar flares, and a series of loops next to the flares. On the right, it displays a zoomed image of the green rectangle at 171, 193, and 211 Å. A thin closed loop (red lines) with one of its bases placed next to the flares is selected. At least two M-class flares have been detected in the area. One nearby flare is about 20" from the footpoint near the flare and positioned at coordinates (576", -115.2'') from the center of the Sun, as observed by the Geostationary Operational Environmental Satellite (GOES). The energy class of this flare near the base is M7.4, with start

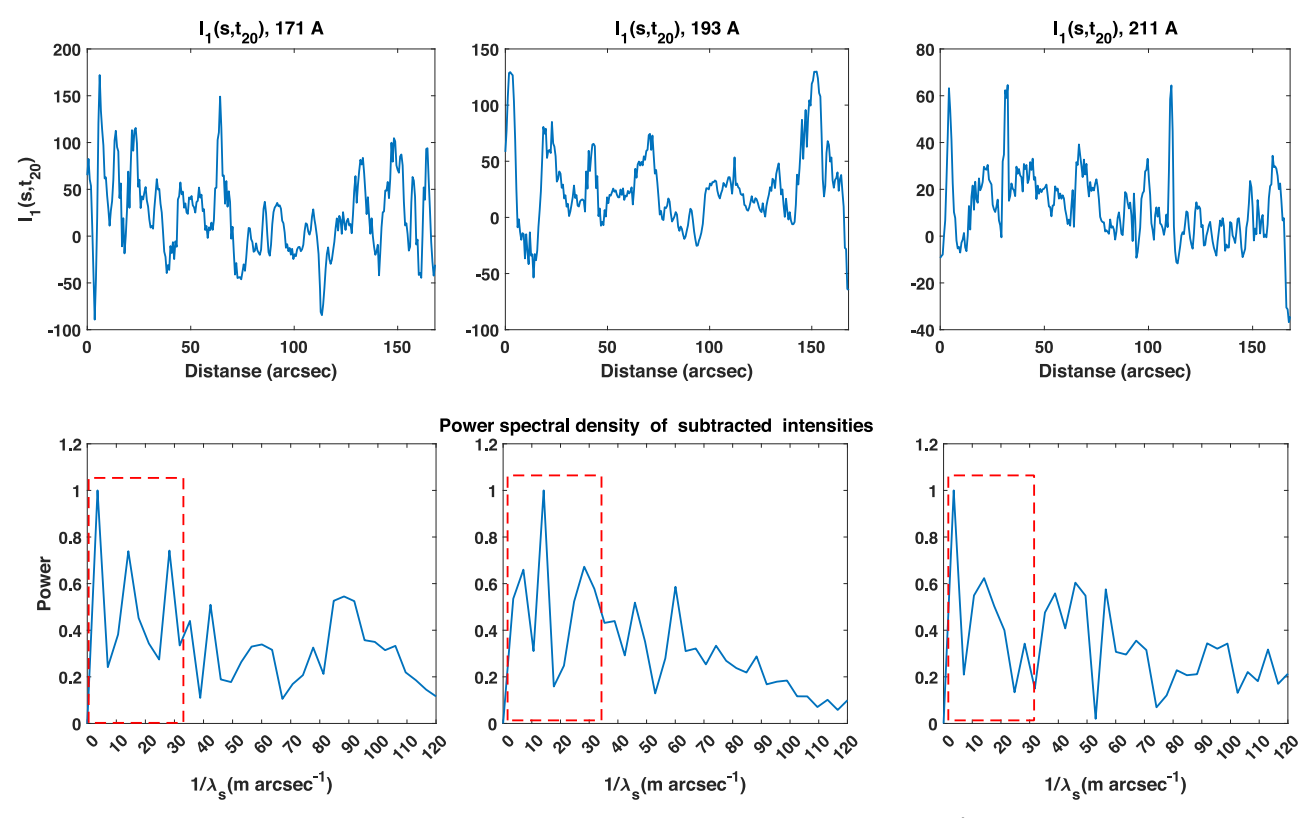


Figure 4. Background-subtracted intensities in terms of distance for the 20th frame in channels 171, 193, and 211 Å are plotted in the top row, from left to right respectively. The spectral power densities of the corresponding time series of intensities are plotted in terms of spatial frequency in the bottom row. In the spectral power density, the spatial frequency range less than 33 milliarcsec⁻¹ ($\lambda_s > 30''$), marked with a red rectangle, was selected and the higher frequencies were removed.

and end times at 12:07:00 UT and 12:20:00 UT, respectively. Another M-class flare is positioned about 97" away from the same footpoint. It occurs at coordinates (44'', -115.2'') relative to the Sun's center, beginning at 12:03:00 UT and concluding at 12:25:00 UT. Images downloaded from the AIA/SDO instrument are at level 1 with a spatial resolution of 0.6". Initial corrections have been applied to the images (see Abedini 2016). These images undergo preprocessing using standard subroutines aia_prep.pro and aia_derot.pro in the SDO package within the SolarSoftWare (SSW) library. The images are rotated to correct the differential rotation error, consequently elevating the image level to 1.5. Figure 1 indicates that flare activity ceases around 12:40:00. To investigate the standing waves in intensity and temperature fluctuations postflare, approximately 250 consecutive images from 12:40 to 13:30 (50 minutes) are selected. To achieve this, the loop is segmented into small macropixels (3×3 pixels in size) along its length. Macropixel sizes are chosen to keep the loop contained during transverse oscillations. The mean intensities of these macropixels in three channels (171, 193, and 211 Å) are analyzed over time to identify longitudinal standing oscillations. Additionally, the extracted intensities from the

six AIA bands are used to calculate the loop's temperature, as detailed in the next section.

3. Data Analysis

To analyze the intensities, a time series of the intensity of macropixels (3×3) pixels in size) of the loop strands is extracted. In the top row of Figure 2, the space-time maps of initial intensities in the channels 171, 193, and 211 Å are shown. The temperature of the coronal loop is calculated using six AIA passbands: 94, 131, 171, 193, 211, and 335 Å. For this purpose, first, the desired loop was straightened into a considered box with a thickness of 16 pixels (macropixel). This has been done by considering the available space around the loop concerning its distance to the neighboring loops. Then, the section along the straightened loop is divided into 3 pixel-wide strips. The differential emission measure (DEM) function in each strip is considered as a single Gaussian function. The DEM peak temperature and the DEMweighted mean temperature are estimated using a spatiallysynthesized Gaussian DEM forward-fitting method (see Aschwanden et al. 2013, 2015; Hosseini Rad et al. 2021; Fathalian et al. 2022). Here, for each AIA temperature filter,

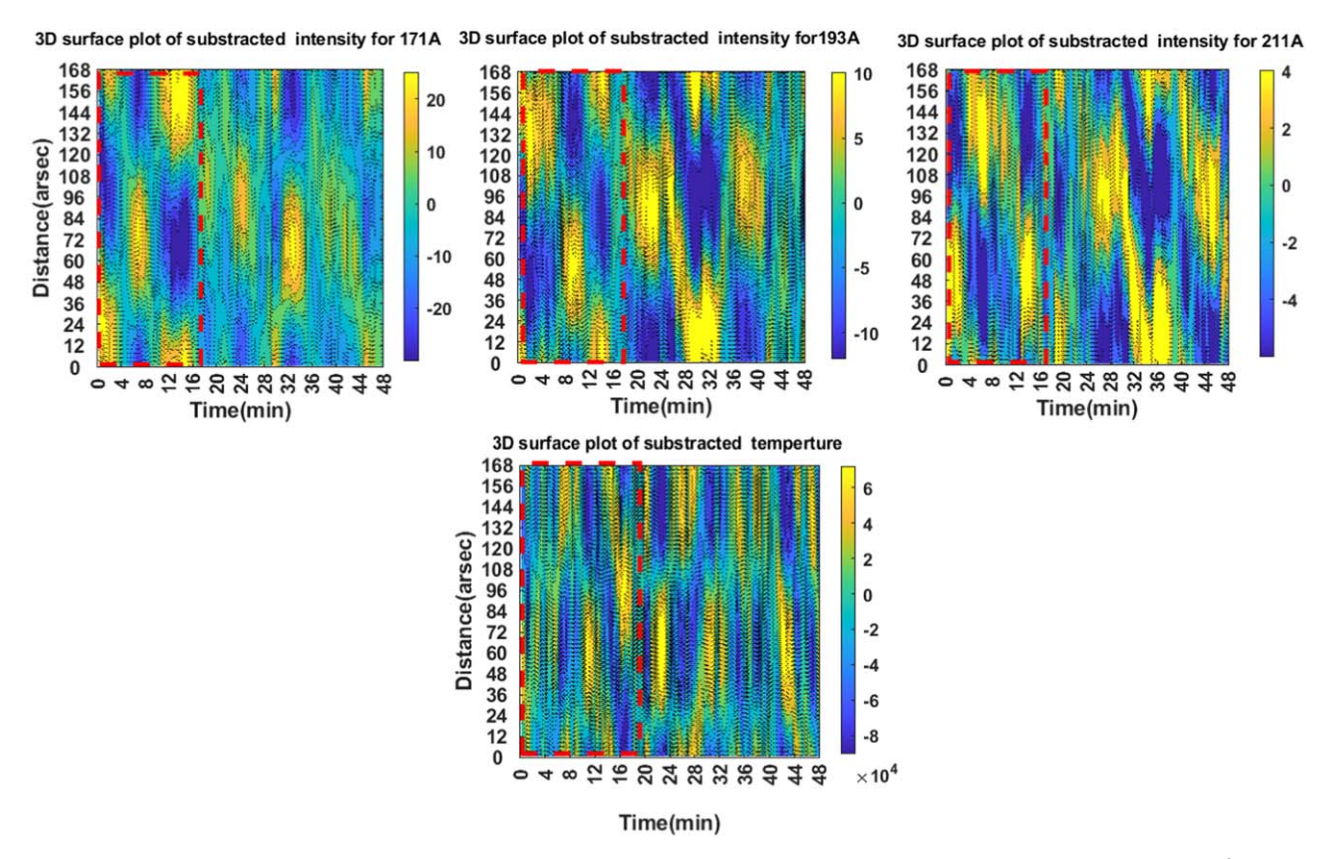


Figure 5. Space-time maps of disturbance intensities at specific filtered spatial frequencies (under 33 milliarcsec⁻¹) in channels 171, 193, and 211 Å (top row, from left to right respectively), and space-time map of filtered spatial frequency disturbance DEM peak temperature (bottom row).

the updated calibration of temperature response functions is applied, utilizing the CHIANTI Version 2019 code available in SSW. The values of the DEM peak temperature along the loop strips are found in the range of 0.51-3.98 MK. In addition, the average value of the DEM peak temperature and the DEM-weighted mean temperature of the coronal loop are found to be 1.89 MK and 2.18 MK, respectively. In the bottom row of Figure 2, the space-time map of the DEM peak temperature is presented. The space-time map of the DEM peak temperature and the DEM-weighted mean temperature indicates that the estimated temperature is low in most strips. Consequently, the coronal loop and its segments are cold ($T < 6 \,\mathrm{MK}$). To observe the disturbance fluctuations of intensities and temperatures, an appropriate background intensity and background temperature are subtracted from the time series of intensities and temperatures obtained from the macropixels using the symmetric running difference method (Abedini 2016).

In the top row of Figure 3, the space-time maps of background-subtracted intensities in channels 171, 193, and 211 Å are shown. In the bottom row, the space-time maps of background-subtracted DEM peak temperatures are displayed.

The figure illustrates the maximum range of intensity amplitudes (in arbitrary units) is approximately 60, while the range of temperature fluctuation amplitudes is around 2.5 million degrees. To enhance the contrast of intensities and temperature oscillations in space-time maps, spatial frequencies higher than 33 milliarcsec⁻¹ (wavelengths less than 30") are initially filtered out from the data. In Figure 4, background-subtracted intensity versus distance for the 20th frame is depicted in the three channels in the upper row. The power spectral densities of these intensities are displayed in the bottom row. Spatial frequencies below 33 milliarcsec⁻¹, marked with a red rectangle, were chosen, while higher frequencies were removed from the data.

In Figure 5, the space-time maps of spatially filtered disturbance intensities at specific spatial frequencies (under 33 milliarcsec⁻¹) (upper row) and disturbance DEM peak temperatures (bottom row) are shown. It is evident that the amplitude of disturbance intensities and temperature fluctuations along the loops varies, indicating standing oscillations along the loop.

Figure 5 displays space-time maps of disturbance intensities at specific filtered spatial frequencies (under 33 milliarcsec⁻¹)

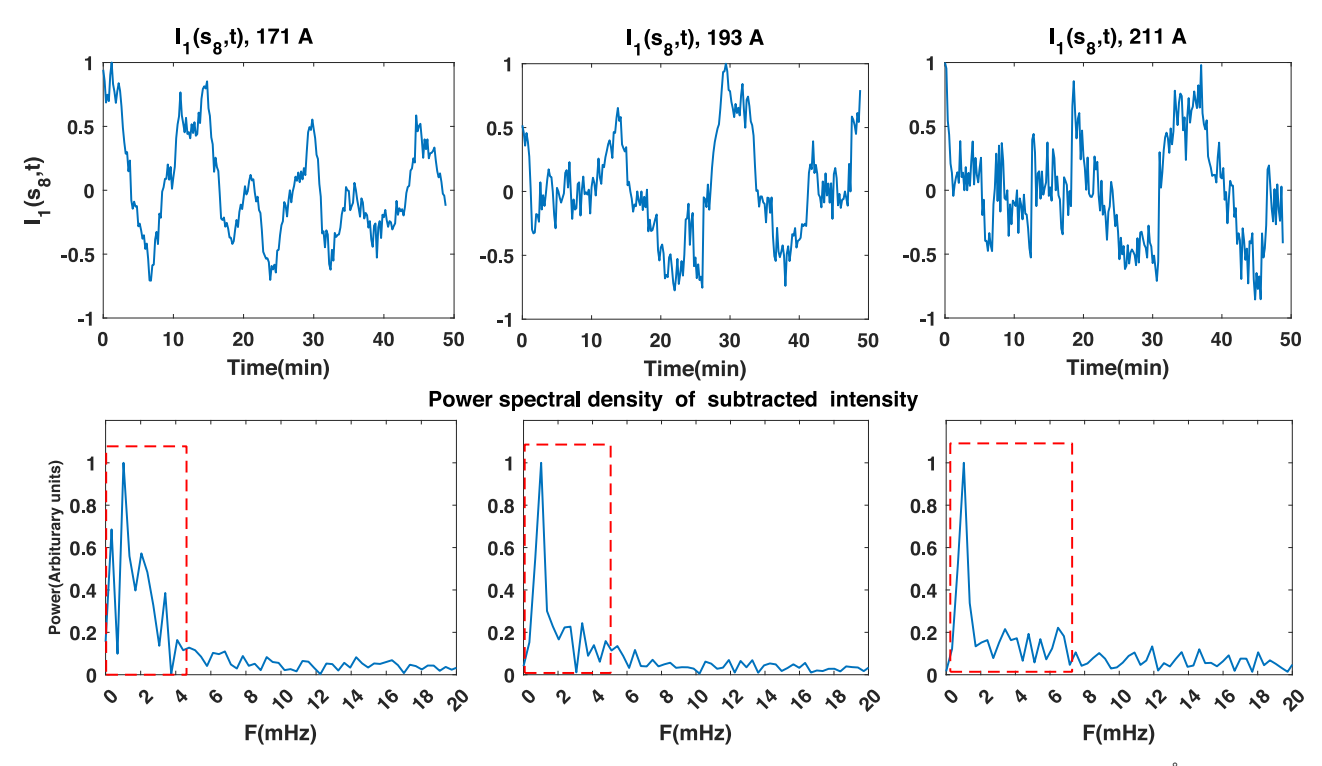


Figure 6. Time series of the normalized and filtered intensities of the 8th macropixel along the loop strands for wavelengths 171, 193, and 211 Å (top row, from left to right respectively). Power spectral densities of intensities vs. frequency (bottom row). Time frequencies below 0.1 amplitude are marked with red rectangles.

in channels 171, 193, and 211 Å (top row, from left to right respectively), and space-time maps of filtered spatial frequencies disturbance temperatures (bottom row). For instance, in the top row of Figure 6, the time series of the normalized intensities of the 8th macropixel counter for the chosen spatial frequencies are displayed over time. Also, in the second row, the power spectral densities are depicted in terms of temporal frequencies. It is evident that in the power spectral densities, there exist higher frequencies which could be attributed to different factors like noise. To improve the contrast of the fluctuation and enhance the accuracy of standing oscillations, temporal frequencies below 0.2 amplitude in the power spectral densities were eliminated. The second row of Figure 6 illustrates these temporal frequencies with amplitudes below 0.1 in the spectral power density, depicted by rectangular lines, that were subsequently removed from the signals. In the top row of Figure 7, space-time maps of normalized and filtered disturbance intensities are shown for selected spatial and temporal frequencies in channels 171, 193, and 211 Å, from left to right respectively. In the bottom row, space-time maps of normalized disturbance DEM peak temperatures are displayed for the same frequencies. In most areas, especially within the region outlined by red rectangles in the space-time maps, the second harmonic oscillations are clearly visible in the disturbance intensities of channels 171,

193, and 211 Å, as well as in the disturbance temperature map. The variation in normalized disturbance intensities across the loop suggests the presence of second harmonic oscillations $(\lambda_s \simeq L/2)$. It is clear from the enhanced maps that along the loop, the locations of the intensities and temperature nodes do not coincide. Instead, intensity antinodes roughly coincide with temperature nodes, and vice versa. There is a phase shift between the time series of temperature and intensities. This shift varied with time and was not constant. Standing waves exhibit an intriguing characteristic where nodes and antinodes appear to gradually shift along the loop. Discrete yellow lines in the space-time maps of normalized intensities and temperatures indicate paths that intersect nodes, with their slopes representing the average speed of node and antinode movement. As can be seen, there are minor differences in the location and slope of the lines through the nodes and antinodes in the space-time maps of intensities and temperatures. These discrepancies may arise from background intensity subtraction, the AIA response functions at different wavelengths for temperature estimation using the DEM method, signal noise, or other factors. Displacements of nodes and antinodes can be caused by factors such as fluid flow from one base near the flare to another or the appearance of additional flares near the loop. The amplitudes of standing oscillation in time intervals roughly 1.5–2 times the oscillation period decrease, then increase once more. The consecutive amplitude decrease and increase may

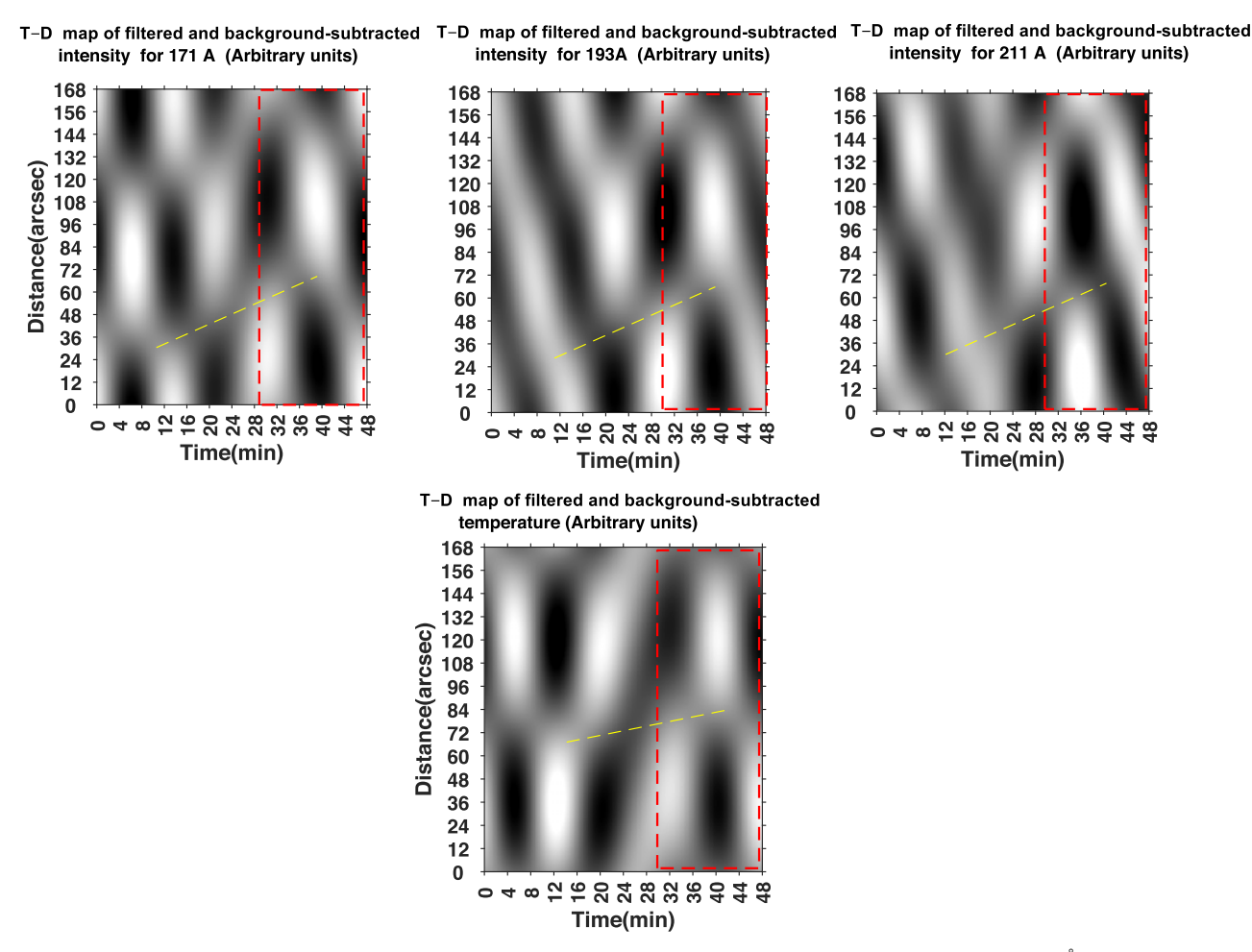


Figure 7. Space-time maps of normalized disturbance intensities for specifically selected frequencies in channels 171, 193, and 211 Å (top row, from left to right respectively). Space-time map of the disrupted DEM peak temperatures for specific frequencies (bottom row). In the regions marked with red rectangles, nodes and anti-nodes of standing oscillations are clearly visible.

stem from momentum transferred by flares striking the loop periodically, while intensity fluctuations from previous flares endure.

To determine the physical characteristics of standing oscillations (waves) like decay time, oscillation period, and initial phase across the loop, intensities at specific frequencies over time were plotted for each macropixel. To calculate the average and range of parameters, a damping cosine function is fitted to the plots. Additionally, to determine the wavelength of the oscillation modes, filtered intensities were plotted against distance along the loop for all frames, then fitted with a cosine function, and the average value and range were computed. For example, in Figure 8, the normalized, background-subtracted and filtered intensities versus time for macropixel 113 in channels 171 and 193 Å, and macropixel 132 along the loop in channel 211 Å are shown (blue lines). To the part of the blue lines that are marked by + symbols, a damping function of the form $e^{\pm}t/\tau_d \cos(2\pi t/P - \phi_0)$ is fitted (red lines). The fit

parameter values are shown on the top of the panels. Normalized intensities along the loop for the 140th frame in channels 171, 193, and 211 Å are depicted in the bottom row (blue lines). To the blue lines that are marked with + symbols, a function of the form $\cos(2\pi z/\lambda_s - \theta_0)$ is fitted, and corresponding fit parameters are written on the panels. The obtained values of these fittings are summarized in Table 1.

4. Discussion and Conclusions

This study aims to detect flare-excited standing slow waves along a thin closed coronal loop near solar flares. For this purpose, the loop's length is initially divided into small segments, each 3×3 pixels in size. Then, the intensity time series of these segments is extracted in channels 171, 193, and 211 Å.

Also, using six AIA passbands, including 94, 131, 171, 193, 211 and 335 Å, the DEM peak temperature time series of strips

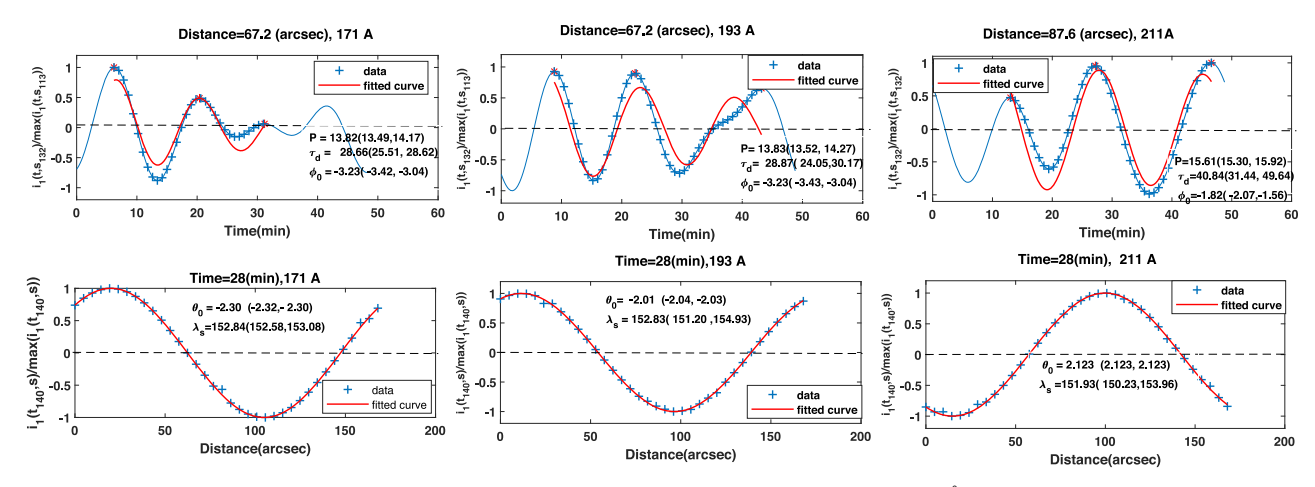


Figure 8. Normalized and background-subtracted intensities vs. time for macropixel 113 in channels 171 and 193 Å, and macropixel 132 along the loop in channel 211 Å are shown (blue lines). To the part of the blue lines that are marked by + symbols, a damping function of the form $e^{\pm}t/\tau_d \cos(2\pi t/P - \phi_0)$ is fitted (red lines). The fit parameter values are shown on the top of the panels. Normalized and background-subtracted intensities of macropixels along the loop for the 140th frame in channels 171, 193, and 211 Å are depicted in the bottom row (blue lines). To the blue lines that are marked with + symbols, a function of the form $\cos(2\pi z/\lambda_s - \theta_0)$ is fitted, and corresponding fit parameters are written on the panels.

 Table 1

 Parameters of Standing Slow Magneto-acoustic Wave

		-8	
Estimated Parameters	Wavelengths		
	171 Å	193 Å	211 Å
$\overline{P_{av}(P_{\min}, P_{\max})}$	14.92 (13.21, 17.56)	14.93	17.81
(minutes)		(11.95, 17.71)	(15.12, 19.15)
$\tau_{av}(\tau_{\min}, \tau_{\max})$	24.02(21.13, 30.71)	30.91	25.60
		(20.68, 35.17)	(12.61, 56.20)
(minutes)			
$Q_{av}(Q_{\min},Q_{\max})$	1.58 (1.18, 1.99)	2.04 (1.15, 2.83)	1.46 (0.83, 2.64)
$\lambda_{av}(\lambda_{\min}, \lambda_{\max})$	134.26 (132.78, 143.05)	132.30	132.28
		(131.18, 132.34)	(129.30, 133.21)
(arcsec)			
$v_{av}(v_{\min}, v_{\max})$	99.52 (83.46, 120.06)	97.95	81.68
		(82.55, 122.84)	(76.86, 97.74)
$(km s^{-1})$			
$T_{pav}(T_{pmin}, T_{pmax})$ (MK)	1.89 (0.51, 3.98)		
$L_{av}(L_{\min}, L_{\max})$ (arcsec)	167.80 (166.46, 171.14)		

along the loop and the DEM-weighted mean temperature of loop are estimated using a spatially-synthesized Gaussian DEM forward-fitting method (see Aschwanden et al. 2013, 2015; Hosseini Rad et al. 2021; Fathalian et al. 2022). An appropriate background intensity and temperature are subtracted from the intensity and temperature time series of the macropixels along

the loop strands. The power spectral densities of the background-subtracted time and space data series are plotted. Based on power spectral density graphs, a specific range of temporal and spatial frequencies is chosen, and the remaining frequencies are eliminated from the intensity and temperature time series. Space-time maps of filtered and background-subtracted intensity and temperature time series are plotted. The distinctive features of standing oscillations in the space-time maps are distinctly evident. Physical parameters of the standing slow waves are determined. The findings of this study are outlined as follows:

- 1. In the enhanced space-time maps of intensities and temperatures, two clear antinodes and one node are visible along the coronal loop, showing standing waves in the loop. The amplitude of these waves systematically decreases and increases as they move from one base to another. Additionally, the average wavelengths calculated in three channels are nearly half the loop length, suggesting it is the second harmonic mode of the standing waves.
- Space-time maps show perturbation intensity nodes and antinodes moving along the loop over time, likely due to plasma flow within the loop driven by energy from flares erupting near a base.
- 3. The average oscillation period ranges from 14 to 18 minutes, while the average damping time of the oscillations is between 24 and 31 minutes.
- 4. These findings align perfectly with previous studies on slow magneto-acoustics (e.g., Taroyan & Bradshaw 2008; Abedini & Safari 2011; Pant et al. 2015; Yuan et al. 2015).

- 5. Space-time maps of the intensities show that the amplitude of standing fluctuations decreases and increases again over time. The re-increase in the amplitude of intensity fluctuations may be caused by successive shocks from flares to the loop while the effects of previous flares are already present in the coronal loop.
- 6. Enhanced space-time maps show the positions of the intensity and temperature nodes do not coincide. Rather, intensity antinodes approximately coincide with temperature nodes, and vice versa. A phase difference exists between the temperature and intensity time series. This phase difference is time-dependent and not constant.
- 7. The average values of the oscillation period, damping time, damping quality (the ratio of damping time to the period), projected wavelength, and projected phase speed of detected standing waves range from 15 to 18 minutes, 24 to 31 minutes, 2" to 1.46", 132" to 134", and 81 to 100 km s⁻¹, respectively.
- 8. The average phase speeds depicted of the calculated oscillations are mostly under $100\,\mathrm{km\ s^{-1}}$. Thus, it is probable that they are caused by slow magneto-acoustic waves.
- The average value of the DEM peak temperature and the DEM-weighted mean temperature of the coronal loop are 1.89 MK and 2.18 MK, respectively. Thus, the loop can be considered relatively cold.
- 10. The average damping quality coefficient calculated shows that these fluctuations are weakly damped. The damping of the fluctuations calculated in this study is low compared to the damping of the fluctuations reported by Ofman & Wang (2002), Wang et al. (2003a, 2015), in the hot coronal loops ($T > 6 \, \text{MK}$) adjacent to the flares. Weak damping may be due to the loop temperature being well below 6 million kelvin, suggesting it is not a hot coronal loop. Therefore, due to the low temperature, the effect of heat conduction in damping is not efficient enough.
- 11. In summary, in this study, flare-excited standing slow magneto-acoustic waves in a thin closed cold coronal loop near the flares were detected more accurately and clearly compared to previous findings, and their physical parameters were determined.

Acknowledgments

The author thanks Prof. Dr. Hossein Safari from the University of Zanjan for his technical support and comments.

References

```
Abedini, A. 2016, Ap&SS, 361, 133
Abedini, A. 2021, JApA., 42, 16
```

```
Abedini, A., & Safari, H. 2011, NewA, 16, 317
Abedini, A., Safari, H., & Nasiri, S. 2012, SoPh, 280, 137
Andries, J., Arregui, I., & Goossens, M. 2005, ApJL, 624, L57
Aschwanden, M. J. 2009, SSRv, 149, 31
Aschwanden, M. J., Boerner, P., Caspi, A., et al. 2015, SoPh, 290, 2733
Aschwanden, M. J., Boerner, P., Schrijver, C. J., & Malanushenko, A. 2013,
   SoPh, 283, 5
Aschwanden, M. J., De Pontieu, B., Schrijver, C. J., & Title, A. M. 2002,
   SoPh. 206, 99
Banerjee, D., Erdélyi, R., Oliver, R., & O'Shea, E. 2007, SoPh, 246, 3
Berghmans, D., & Clette, F. 1999, SoPh, 186, 207
Bryans, P., McIntosh, S. W., De Moortel, I., & De Pontieu, B. 2016, ApJL,
  829, L18
De Moortel, I., Ireland, J., & Walsh, R. W. 2000, A&A, 355, L23
DeForest, C. E., & Gurman, J. B. 1998, ApJL, 501, L217
Fathalian, N., Somayeh Hosseini Rad, S., Alipour, N., & Safari, H. 2022,
  RAA, 22, 035015
Hosseini Rad, S., Alipour, N., & Safari, H. 2021, ApJ, 906, 59
Jiao, F., Xia, L., Li, B., et al. 2015, ApJL, 809, L17
Krishna Prasad, S., Banerjee, D., & Van Doorsselaere, T. 2014, ApJ, 789, 118
Kumar, P., Innes, D. E., & Inhester, B. 2013, ApJL, 779, L7
Kumar, P., Nakariakov, V. M., & Cho, K.-S. 2015, ApJ, 804, 4
Kupriyanova, E. G., Melnikov, V. F., & Shibasaki, K. 2013, SoPh, 284, 559
Mandal, S., Yuan, D., Fang, X., et al. 2016, ApJ, 828, 72
Marsh, M. S., Walsh, R. W., & Plunkett, S. 2009, ApJ, 697, 1674
Nightingale, R. W., Aschwanden, M. J., & Hurlburt, N. E. 1999, SoPh,
  190, 249
Nisticò, G., Polito, V., Nakariakov, V. M., & Del Zanna, G. 2017, A&A,
  600, A37
Ofman, L. 2005, SSRv, 120, 67
Ofman, L., Nakariakov, V. M., & DeForest, C. E. 1999, ApJ, 514, 441
Ofman, L., Romoli, M., Poletto, G., Noci, G., & Kohl, J. L. 1997, ApJL,
  491. L111
Ofman, L., & Wang, T. 2002, ApJL, 580, L85
Pant, V., Dolla, L., Mazumder, R., et al. 2015, ApJ, 807, 71
Pant, V., Tiwari, A., Yuan, D., & Banerjee, D. 2017, ApJL, 847, L5
Samanta, T., Pant, V., & Banerjee, D. 2015, ApJL, 815, L16
Selwa, M., Murawski, K., & Solanki, S. K. 2005, A&A, 436, 701
Sigalotti, L. D. G., Mendoza-Briceño, C. A., & Luna-Cardozo, M. 2007, SoPh,
  246, 187
Taroyan, Y., & Bradshaw, S. 2008, A&A, 481, 247
Taroyan, Y., & Erdélyi, R. 2009, SSRv, 149, 229
Taroyan, Y., Erdélyi, R., Doyle, J. G., & Bradshaw, S. J. 2005, A&A, 438, 713
Taroyan, Y., Erdélyi, R., Wang, T. J., & Bradshaw, S. J. 2007, ApJL,
  659, L173
Tsiklauri, D., Nakariakov, V. M., Arber, T. D., & Aschwanden, M. J. 2004,
    &A, 422, 351
Van Doorsselaere, T., Brady, C. S., Verwichte, E., & Nakariakov, V. M. 2008,
  A&A, 491, L9
Van Doorsselaere, T., De Groof, A., Zender, J., Berghmans, D., &
  Goossens, M. 2011, ApJ, 740, 90
Wang, T. 2011, SSRv, 158, 397
Wang, T., Innes, D. E., & Qiu, J. 2007, ApJ, 656, 598
Wang, T., Ofman, L., Sun, X., Provornikova, E., & Davila, J. M. 2015, ApJL,
  811, L13
Wang, T., Solanki, S. K., Curdt, W., Innes, D. E., & Dammasch, I. E. 2002,
  ApJL, 574, L101
```

Wang, T. J., Ofman, L., & Davila, J. M. 2009a, ApJ, 696, 1448

Wang, T. J., Solanki, S. K., Curdt, W., et al. 2003a, A&A, 406, 1105Wang, T. J., Solanki, S. K., Innes, D. E., Curdt, W., & Marsch, E. 2003b,

Wang, T. J., Ofman, L., Davila, J. M., & Mariska, J. T. 2009b, A&A, 503, L25

Wang, T. J., Solanki, S. K., Innes, D. E., & Curdt, W. 2005, A&A, 435, 753

Yuan, D., Van Doorsselaere, T., Banerjee, D., & Antolin, P. 2015, ApJ,

A&A, 402, L17

807, 98